

# Photocatalytic Hydrogen Generation by Monodisperse TiO<sub>2</sub> Nanoparticles Singly and Dually Doped with Niobium and Tantalum

Nhat M. Ngo, Minh Dang Nguyen, Hung-Vu Tran, Riddhiman Medhi, Jong Moon Lee, and T. Randall Lee\*



Cite This: *ACS Appl. Nano Mater.* 2025, 8, 4841–4851



Read Online

ACCESS |



Metrics & More



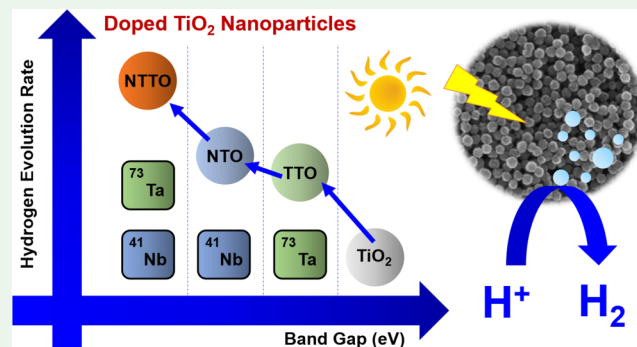
Article Recommendations



Supporting Information

**ABSTRACT:** Despite the many advantageous characteristics of an excellent photocatalyst for large-scale applications, some critical challenges still hinder the prospects of titanium dioxide. While judicious doping and nanoscale fabrication offer logical avenues for improvement, most of these methods require complex processes under demanding conditions, which are undesirable for scale-up. In the work reported here, highly monodisperse spherical nanoparticles of undoped, singly doped (NTO and TTO), and dually doped (NTTO) anatase TiO<sub>2</sub> using niobium and tantalum as dopants were prepared by scalable methods under mild conditions. The doped TiO<sub>2</sub> nanoparticles showed reduced band gap energies and adjustable suppressions of the rate of electron–hole recombination, with the largest reductions observed for the heretofore unreported dually doped NTTO nanoparticles. Furthermore, the introduction of Nb and/or Ta dopants into the TiO<sub>2</sub> lattice also substantially improved the photocatalytic hydrogen evolution rates and quantum yields, with the NTTO nanoparticles achieving the highest performance in both metrics. Importantly, all these nanoparticles maintained high stability after multiple photocatalytic hydrogen evolution test cycles, indicating that doped TiO<sub>2</sub> nanoparticles have significant potential for use in photocatalytic fuel generation and related optoelectronic applications.

**KEYWORDS:** titanium dioxide, TiO<sub>2</sub>, nanoparticles, niobium, Nb, tantalum, Ta, semiconductor, doped, dopant, band gap, electron–hole recombination, photocatalysis, hydrogen evolution



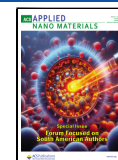
the successful incorporation of various dopants into TiO<sub>2</sub> nanomaterials to achieve optical and electronic properties required for applications in photocatalysis,<sup>15</sup> photovoltaics,<sup>16</sup> and optoelectronics.<sup>17,18</sup> Despite advances in synthetic methods, such as solvothermal,<sup>19,20</sup> sol–gel,<sup>21,22</sup> hydrothermal,<sup>23</sup> molten salt flux,<sup>24</sup> and electrochemical techniques,<sup>25</sup> for producing doped TiO<sub>2</sub> nanoparticles, these methods often require complex and demanding conditions. Niobium (Nb)- and tantalum (Ta)-doped TiO<sub>2</sub> films, which possess high conductivity<sup>26,27</sup> and visible transparency,<sup>26,28</sup> have emerged as promising alternatives to indium tin oxide (ITO) for transparent conducting oxide (TCO) applications.<sup>29,30</sup> This enhancement in conductivity,<sup>31,32</sup> especially when coupled with the high surface area of nanoscale structures,<sup>32</sup> is also advantageous for photocatalysis and gas sensing applications.

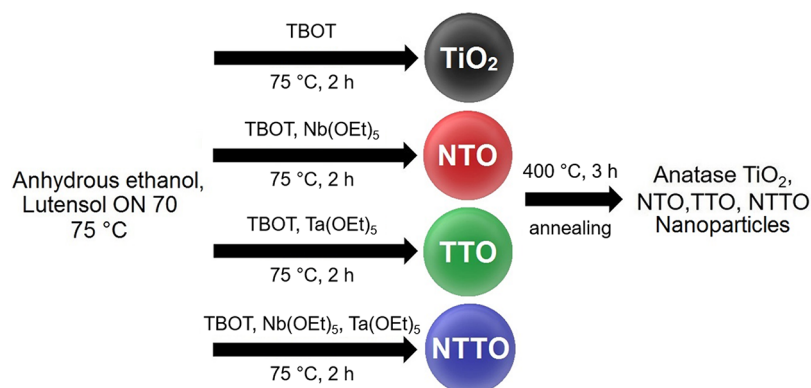
## INTRODUCTION

The rapidly growing demand for sustainable energy sources and increasing environmental concerns about fossil fuels have spurred the development of efficient and abundant photocatalysts for solar-powered hydrogen generation.<sup>1</sup> Since the seminal report by Fujishima and Honda in 1972,<sup>2</sup> semiconductor titanium dioxide (TiO<sub>2</sub>) has been extensively studied for its ability to convert solar radiation into high-energy-density fuels, such as hydrogen, which produces minimal polluting byproducts (e.g., water).<sup>3–6</sup> Although TiO<sub>2</sub> possesses numerous advantages including high stability,<sup>7</sup> nontoxicity,<sup>8</sup> and material abundance, its large band gap energy requiring UV light for activation<sup>9</sup> and high electron–hole recombination rate<sup>9</sup> remain major challenges for large-scale applications. Advances in nanoscience and technology have highlighted the potential of nanoscale structures for catalytic applications due to their high surface-to-volume ratio and quantum confinement effects,<sup>10</sup> offering new avenues to overcome these challenges.

Doping has been recognized as an effective strategy to reduce the band gap and enhance the absorption coefficients of semiconductors.<sup>11</sup> Numerous studies have demonstrated<sup>12–14</sup>

**Received:** January 20, 2025  
**Revised:** February 5, 2025  
**Accepted:** February 6, 2025  
**Published:** February 25, 2025



Scheme 1. Synthesis of TiO<sub>2</sub>, NTO, TTO, and NTTO Nanoparticles<sup>a</sup>

<sup>a</sup>**Abbreviations:** TBOT: titanium(IV) butoxide, Nb(OEt)<sub>5</sub>: niobium(V) ethoxide, Ta(OEt)<sub>5</sub>: tantalum(V) ethoxide, NTO: niobium-doped TiO<sub>2</sub>, TTO: tantalum-doped TiO<sub>2</sub>, NTTO: niobium/tantalum-codoped TiO<sub>2</sub>.

However, the synthesis of Nb-<sup>33–35</sup> and Ta-doped<sup>35,36</sup> TiO<sub>2</sub> nanoparticles often involves challenging synthetic procedures or fails to ensure precise control over nanoparticle properties. Recently, several encouraging results have been reported by other researchers for Nb-doped TiO<sub>2</sub> and Ta-doped TiO<sub>2</sub> nanoparticles.<sup>33,37–39</sup> However, the fabrication of highly uniform nanoparticles with homogeneous spherical morphology and monodisperse particle size for doped TiO<sub>2</sub> remains a significant challenge. Therefore, there is a critical need to develop more facile methods for producing Nb-, Ta-, and other element-doped TiO<sub>2</sub> nanoparticles that are suitable for scaling up with monodisperse quality. Moreover, codoping TiO<sub>2</sub> with multiple elements has been shown to not only reduce the band gap but also enhance the optical properties, providing significant benefits for solar-powered applications.<sup>11,40,41</sup>

In this report, we developed a rapid, facile, and scalable (gram-level) synthesis method for doped particle catalysts. Specifically, we report the synthesis of anatase TiO<sub>2</sub> nanoparticles doped with various combinations of Nb and Ta, including undoped TiO<sub>2</sub>, singly doped such as Nb-doped TiO<sub>2</sub> (NTO), Ta-doped TiO<sub>2</sub> (TTO), and the previously unreported Nb/Ta codoped TiO<sub>2</sub> (NTTO), as specified in Scheme 1. These nanoparticles were synthesized via a controlled hydrolytic process under mild conditions, yielding highly monodisperse, spherical nanoparticles with uniform dopant distribution within the crystalline matrix. Notably, by adjusting the concentrations of Nb and Ta dopants, we successfully controlled the electron–hole recombination rates in TiO<sub>2</sub>, with the NTTO nanoparticles showing the most pronounced suppression. Furthermore, Nb and Ta doping decreased the optical band gap of TiO<sub>2</sub> nanoparticles, with the largest reduction observed in the dually doped NTTO particles. Photocatalytic hydrogen generation studies in the absence of any cocatalyst, such as Pt, Pd, and Ru, showed significant increases in hydrogen evolution rates for the doped compared to the pristine TiO<sub>2</sub> nanoparticles. Beneficially, the doped TiO<sub>2</sub> nanocatalysts also exhibited a high degree of photostability in cyclability tests. Overall, the enhanced hydrogen evolution rates, combined with the good scalability and mild conditions of the synthetic methods, endow the NTO, TTO, and NTTO nanoparticles with great potential for photocatalytic fuel generation. Additionally, the tunable photoluminescence (PL) responses and optical band gaps of these doped nanoparticles broaden their applicability to

optoelectronic,<sup>42</sup> photovoltaic,<sup>43</sup> gas sensing,<sup>44</sup> or biomedical<sup>45</sup> applications.

## EXPERIMENTAL SECTION

**Materials.** Titanium(IV) butoxide (97% purity, TBOT), niobium(V) ethoxide (99.95% purity, Nb(OEt)<sub>5</sub>), tantalum(V) ethoxide (99.98% purity, Ta(OEt)<sub>5</sub>), and anhydrous ethylene glycol (99.8% purity) were purchased from Sigma-Aldrich. Lutensol ON 70 was obtained from BASF SE Inc. Anhydrous ethanol (200 proof) was purchased from Decon Laboratories Inc. Deionized water with a resistivity of 18.2 MΩ-cm was obtained from the Milli-Q Academic water system from Millipore Corporation. Sodium hydroxide was purchased from Macron Fine Chemicals. Ultrahigh purity compressed argon gas was purchased from Matheson Tri-Gas Inc. All glassware was cleaned with piranha solution (3:1 concentrated sulfuric acid: 30% hydrogen peroxide) and aqua regia solution (3:1 concentrated hydrochloric acid: nitric acid) for at least 1 h, then dried in an oven at 150 °C and allowed to cool prior to use.

**Synthesis of Nanoparticles.** Scheme 1 outlines the synthetic strategy and subsequent heat treatment for TiO<sub>2</sub>, NTO, TTO, and NTTO nanoparticles. To prepare the stock solutions, 100 μL of TBOT, 10 μL of Nb(OEt)<sub>5</sub>, and 10 μL of Ta(OEt)<sub>5</sub> were each mixed with 10 mL of fresh anhydrous ethanol, respectively. The reaction conditions for synthesizing both undoped and doped TiO<sub>2</sub> nanoparticles are summarized in Table S1.

**Synthesis of TiO<sub>2</sub> Nanoparticles.** The formation of TiO<sub>2</sub> nanoparticles was achieved by hydrolyzing TBOT in an ethanolic solution containing Lutensol ON 70 surfactant and carefully controlling the water content in the reaction mixture. Initially, 352 μL of 0.1 M Lutensol ON 70 was mixed with 14 mL of anhydrous ethanol and heated to 75 °C for 15 min (mixture A). An aliquot of 1 mL TBOT stock solution was then added to mixture A, followed by the addition of 400 μL of deionized water. This mixture was kept at 75 °C for 2 h under vigorous magnetic stirring. Within 10 min of adding deionized water, the solution changed from transparent to translucent, indicating the nucleation of TiO<sub>2</sub> nanoparticles. After 2 h of stirring at 75 °C and subsequent cooling to room temperature for 1 h, the fully grown nanoparticles were collected by centrifugation at 7000 rpm for 15 min. The nanoparticles were then washed with deionized water and centrifuged four times to remove any residual reagents. Finally, the nanoparticles were redispersed in ethanol for storage.

**Synthesis of Niobium-Doped TiO<sub>2</sub> (NTO) Nanoparticles.** Nb-doped TiO<sub>2</sub> can be prepared by concurrent hydrolysis of TBOT and Nb(OEt)<sub>5</sub> in an ethanolic solution. For a typical synthesis aiming for 2 atom % Nb doping, 319 μL of 0.1 M Lutensol ON 70 ethanolic solution was mixed with 13 mL of anhydrous ethanol and heated to 75 °C for 15 min (mixture B). Subsequently, a mixture of 1 mL of TBOT and 0.588 mL of Nb(OEt)<sub>5</sub> stock solution was injected into

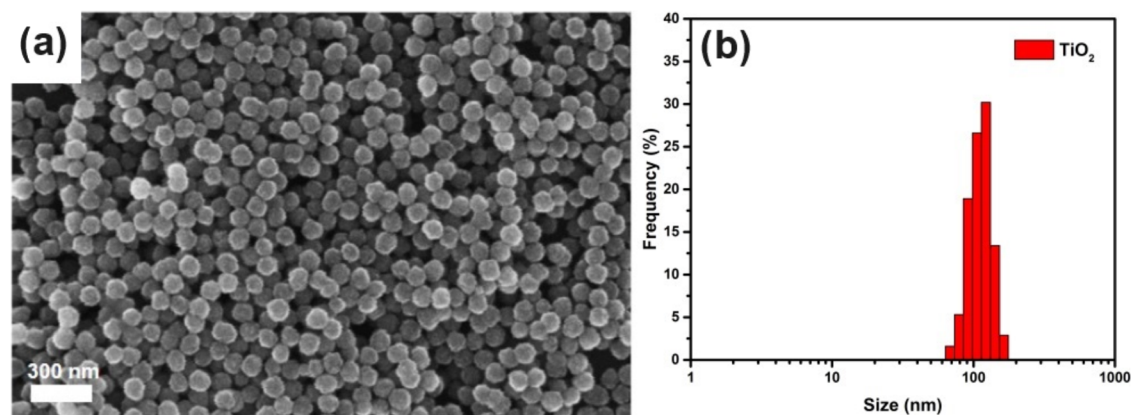


Figure 1. (a) SEM image and (b) size distribution of TiO<sub>2</sub> nanoparticles.

mixture B, followed by the addition of 400  $\mu\text{L}$  of deionized water after 1 min. Within 15 min, the solution became translucent, indicating the formation of NTO nanoparticles, which were fully grown after 2 h of heating at 75  $^{\circ}\text{C}$ . After cooling to room temperature for 1 h with vigorous stirring, the nanoparticles were collected by centrifugation at 7000 rpm for 15 min. The concentration of Nb doping can be controlled by adjusting the ratio of TBOT to Nb(OEt)<sub>5</sub>.

**Synthesis of Tantalum-Doped TiO<sub>2</sub> (TTO) Nanoparticles.** The synthesis of TTO nanoparticles was achieved through the concurrent hydrolysis of TBOT and Ta(OEt)<sub>5</sub> in ethanol. To prepare TTO nanoparticles with doping concentration of 4 atom % Ta, a mixture containing 350  $\mu\text{L}$  of 0.1 M Lutensol ON 70 ethanolic solution and 12.5 mL of anhydrous ethanol was heated to 75  $^{\circ}\text{C}$  for 15 min (mixture C). Following this, a mixture of 1.5 mL of TBOT and 1 mL of Ta(OEt)<sub>5</sub> stock solution were then injected into mixture C, followed by the addition of 400  $\mu\text{L}$  of deionized water after 2 min. Within 15 min of water addition, the solution became translucent, indicating the initiation of TTO nanoparticle formation. The reaction was maintained at 75  $^{\circ}\text{C}$  for 2 h, allowing the nanoparticles to fully grow. After cooling the solution to room temperature for 1 h with continuous stirring, the nanoparticles were collected by centrifugation at 7000 rpm for 15 min. The concentration of Ta doping can be adjusted by varying the ratio of TBOT to Ta(OEt)<sub>5</sub>.

**Synthesis of Niobium/Tantalum-Codoped TiO<sub>2</sub> (NTTO) Nanoparticles.** TiO<sub>2</sub> nanoparticles codoped with Nb and Ta (NTTO) were synthesized through concurrent hydrolysis of TBOT, Nb(OEt)<sub>5</sub>, and Ta(OEt)<sub>5</sub>. In a synthesis aimed at achieving maximum doping levels simultaneously of both Nb and Ta, a mixture containing 25 mL of fresh anhydrous ethanol and 640  $\mu\text{L}$  of 0.1 M Lutensol ON 70 ethanolic solution was heated to 75  $^{\circ}\text{C}$  for 25 min (mixture D). Then, a solution consisting of 3 mL of TBOT, 1.765 mL of Nb(OEt)<sub>5</sub>, and 2 mL of Ta(OEt)<sub>5</sub> stock solutions was well mixed and injected into mixture D, with 0.8 mL of deionized water added after 2 min. The solution became translucent within 15 min, indicating the nucleation of NTTO seeds. The hydrolysis reaction proceeded for 2 h at 75  $^{\circ}\text{C}$ . The nanoparticle solution was subsequently cooled to room temperature for 1 h and the nanoparticles were isolated by centrifugation at 7000 rpm for 15 min.

**Heat Treatment of Nanoparticles.** The synthesized undoped and doped TiO<sub>2</sub> nanoparticles are amorphous and can be transformed into the crystalline anatase phase through proper heat treatment. Initially, the nanoparticles were washed five times with centrifugation at 7000 rpm for 15 min each cycle and then dispersed in ethanol in a clean 20 mL glass vial. The dispersion was dried at 70  $^{\circ}\text{C}$  overnight in an oven. The glass vial containing the dried amorphous nanoparticles was then placed in a preheated furnace and subjected to heat treatment at 400  $^{\circ}\text{C}$  for 3 h. After cooling to room temperature, the now crystallized anatase TiO<sub>2</sub> nanoparticles were redispersed in deionized water using sonication for 60 min.

**Characterization Methods.** All synthesized nanoparticles were imaged using a LEO-1525 scanning electron microscope (SEM)

operating at 15 kV and 5.5 mm working distance. For SEM analysis, samples were drop-cast onto clean silicon surfaces and then dried at 60  $^{\circ}\text{C}$  for 2 h prior to imaging. The size distributions of the nanoparticles were determined by dynamic light scattering (DLS) using a Malvern Zetasizer ZEN3600, employing a 10 mW, 632.8 nm laser. The Zetasizer ZEN3600 was also utilized to measure the  $\zeta$  potentials of the nanoparticles using a DTS1070 folded capillary zeta cell. For both DLS and  $\zeta$  potential measurements, all nanoparticle samples were dispersed in deionized water supplied by the Milli-Q Academic water system. Crystallinity was assessed with an X'Pert powder X-ray diffractometer (XRD) with a Cu K $\alpha$  X-ray source at 45 kV and 30 mA across a  $2\theta$  range of 20 to 80 $^{\circ}$ . The XRD data were analyzed using PANalytical HighScore Plus software after background signal subtraction. Crystallite sizes were calculated using the Scherrer equation, based on peak positions and the full width at half-maximum (fwhm) provided by the software. For XRD analysis, highly concentrated nanoparticle solutions were drop-cast onto amorphous glass slides and dried at 60  $^{\circ}\text{C}$  for 2 h. Elemental composition was investigated via energy-dispersive X-ray spectroscopy (EDX) using a JEOL JEM-2010 FX scanning transmission electron microscope (STEM) operating at 200 kV. Samples for EDX were prepared on 300-mesh holey carbon-coated copper grids and dried at 60  $^{\circ}\text{C}$  for 4 h. Surface elemental measurements were performed with a PHI X-ray photoelectron spectroscopy (XPS) system, featuring a monochromatic Al K $\alpha$  X-ray source with an emission current of 10 mA and a 15 kV emission bias. The C 1s peak was used for calibration. XPS samples were prepared by depositing highly concentrated nanoparticle solutions onto clean silicon wafers and drying at 60  $^{\circ}\text{C}$  for 6 h. Optical properties were analyzed through diffuse reflectance spectra (DRS) obtained with a Cary 5000 UV–vis–NIR spectrometer from Agilent Technologies. Photoluminescence measurements were conducted using a PerkinElmer LS-55 fluorescence spectrometer with an excitation wavelength of 350 nm, employing a 430 nm high-pass optical filter to minimize spectral noise.

**Photocatalytic Hydrogen Generation Test.** Photocatalytic hydrogen evolution reaction (HER) tests for the nanoparticle samples were conducted using a custom-made system with a customized pico solar simulator from G2 V Optics serving as the illumination source. The hydrogen generated was detected by a GOW-MAC series 400-P thermal conductivity gas chromatograph equipped with an 8 ft  $\times$  1/8 in stainless steel column packed with 3  $\text{\AA}$  molecular sieves. The temperatures for the column, detector, and injector were set at 80, 120, and 120  $^{\circ}\text{C}$ , respectively. Ultrahigh purity argon in a pressurized gas cylinder was used as the carrier gas for the chromatography system. In a typical test, 20 mg of nanoparticles were dispersed in 10 mL of a 10% ethylene glycol aqueous solution, which had been adjusted to pH 11, in a customized glass reaction flask. This solution was then purged with ultrahigh purity compressed argon gas for 15 min before being illuminated by the solar simulator. The amount of gas produced was monitored by a digital pressure transducer connected to the reaction flask. Gas samples were extracted through

a sampling port and analyzed with the GOW-MAC gas chromatograph, using a 0.5 mL Hamilton glass syringe for sampling. We note that without ethylene glycol, no hydrogen was generated. For the cyclability tests, the nanoparticle photocatalyst was collected by centrifugation at 7000 rpm for 15 min and rinsed three times with deionized before being reused in subsequent cycles.

## RESULTS AND DISCUSSION

**Synthesis and Morphological Analysis of the Nanoparticles.** We developed a convenient one-step wet chemistry method for synthesizing undoped and doped TiO<sub>2</sub> nanoparticles (Scheme 1). The resulting nanoparticles are sphere-like with average sizes of ~118 nm for TiO<sub>2</sub> (Figure 1a), ~106 nm for NTO, ~98 nm for TTO, and ~104 nm for NTTO (Figure S1a–c), respectively. The nanoparticle size can be tuned by adjusting the concentrations of the stock solutions. Additionally, the synthesized nanoparticles are highly monodisperse, as evidenced by the DLS size distribution profiles in Figures 1b and S1d–f, which corresponds well with the morphologies observed in the SEM images. It has been found critical to preheat the mixture of ethanol and Lutensol ON 70 at 75 °C for 10–15 min to achieve a high degree of monodispersity. This preheating step accelerates the hydrolytic reaction and increases the TiO<sub>2</sub> concentration rapidly, leading to supersaturation.<sup>46</sup> This process minimizes the nucleation period and effectively separates nucleation from growth, resulting in a narrower size distribution of the nanoparticles.<sup>47</sup> While temperatures above 75 °C might further enhance supersaturation and monodispersity, we chose 75 °C to avoid the need for a condenser, which could alter solution concentrations over time and introduce potential contaminants. For doped TiO<sub>2</sub> nanoparticles, reducing the surfactant and increasing the precursor quantities were necessary to match the sizes as undoped variants. This adjustment likely compensates for the lattice strain introduced by doping atoms, which makes the formation of doped TiO<sub>2</sub> seeds more challenging than undoped ones.<sup>48</sup> This nucleation hurdle, marked by a longer time for the solutions to turn translucent, can be overcome by adjusting the reactant concentrations as previously mentioned. Importantly, this synthesis process can be scaled up 10-fold without significantly affecting the morphological characteristics of the nanoparticles.

**Effect of Nb and Ta Doping on TiO<sub>2</sub> Nanoparticle Surface Charge.** Doping TiO<sub>2</sub> with Nb did not significantly change the surface charge magnitude of NTO (−16.3 mV) when compared to undoped TiO<sub>2</sub> (+16.8 mV). However, Ta doping markedly increased the  $\zeta$  potential magnitude of TTO (−22.8 mV) and NTTO (−32.6 mV) as indicated in Table S2. This increase in the  $\zeta$  potential magnitude enhances the colloidal stability of these nanoparticles. Moreover, doping with Nb and Ta shifted the  $\zeta$  potentials of the doped TiO<sub>2</sub> nanoparticles to negative values, contrary to the positive value observed in undoped TiO<sub>2</sub>, exhibiting the impact of doping on surface charge polarity (Table S2). This shift from positive to negative enhances the electrostatic attraction of protons (H<sup>+</sup>) to the reaction sites on the surfaces of the doped TiO<sub>2</sub> nanoparticles. As a result, the doped TiO<sub>2</sub> nanoparticles demonstrated heightened photocatalytic activities compared to their undoped counterparts, particularly evident in hydrogen evolution reactions, which will be discussed in detail subsequently in the manuscript. These findings are in alignment with previously reported studies,<sup>49,50</sup> supporting the beneficial effects of doping on photocatalytic performance.

Overall, our synthesis methods have produced highly monodisperse, spherical undoped, Nb-doped, Ta-doped, and Nb/Ta codoped TiO<sub>2</sub> nanoparticles, ranging in size from ~98 to ~118 nm. Importantly, the doped nanoparticles exhibited more negative surface charges and higher surface charge magnitudes compared to the undoped TiO<sub>2</sub>, offering potential advantages for photocatalytic and various other applications.<sup>49,50</sup>

**Crystallographic Analysis.** Powder X-ray diffraction (XRD) measurements were performed on the crystallized nanoparticle samples to elucidate their crystalline characteristics (Figure 2). The XRD pattern of anatase TiO<sub>2</sub>

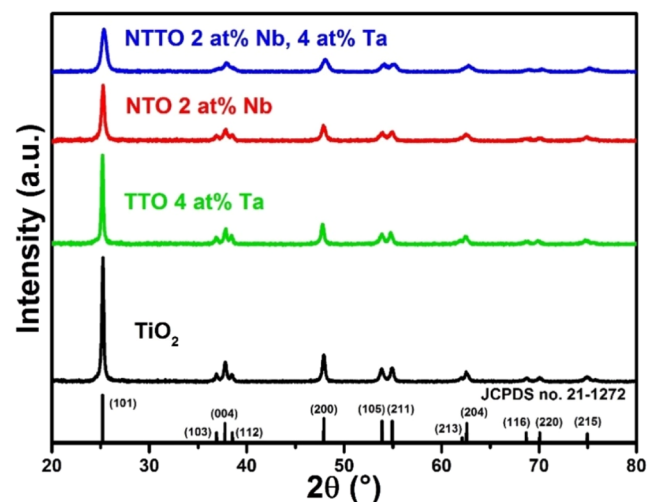


**Figure 2.** Powder XRD patterns of TiO<sub>2</sub>, TTO, NTO, and NTTO nanoparticles with reference lines of anatase TiO<sub>2</sub>.

nanoparticles displayed distinct peaks at  $2\theta$  angles of 25.25, 36.90, 37.76, 38.52, 47.91, 53.89, 54.95, 62.01, 62.60, 68.77, 70.77, and 74.95°. These peaks correspond to the (101), (103), (004), (112), (200), (105), (211), (213), (204), (116), (220), and (215) crystallographic planes, respectively, confirming the presence of the anatase phase of TiO<sub>2</sub> (JCPDS no. 21–1272). For the doped nanoparticles, including TTO (4 atom % Ta), NTO (2 atom % Nb), and NTTO (4 atom % Ta and 2 atom % Nb), the XRD patterns showed similarities to those of undoped TiO<sub>2</sub> nanoparticles (Figure 2 and Table S3). This resemblance is attributed to the minimal differences in atom radii between Nb, Ta, and Ti, which result in negligible lattice distortion and, consequently, an insignificant shift in diffraction peaks. Furthermore, the incorporation of dopants into the TiO<sub>2</sub> lattice at low concentrations means any potential peak shifts fall within the range of instrumental error. Crystallite size calculations for all nanoparticles, derived from the XRD data using the Scherrer equation, are presented in Table S4. The crystallite size of undoped TiO<sub>2</sub> nanoparticles was ~40 nm, while TTO, NTO, and NTTO nanoparticles exhibited smaller crystallite sizes of ~33, ~25, and ~15 nm, respectively. These results are consistent with the observed lower intensities and broader, less distinct XRD peaks for doped nanoparticles when compared to undoped TiO<sub>2</sub>. This indicates the difficulty of the nucleation process due to the inclusion of dopant atoms into the TiO<sub>2</sub> lattice, as discussed in the synthesis process above.

**Compositional Analysis of Doped TiO<sub>2</sub> Nanoparticles.** The compositional characteristics and elemental distributions

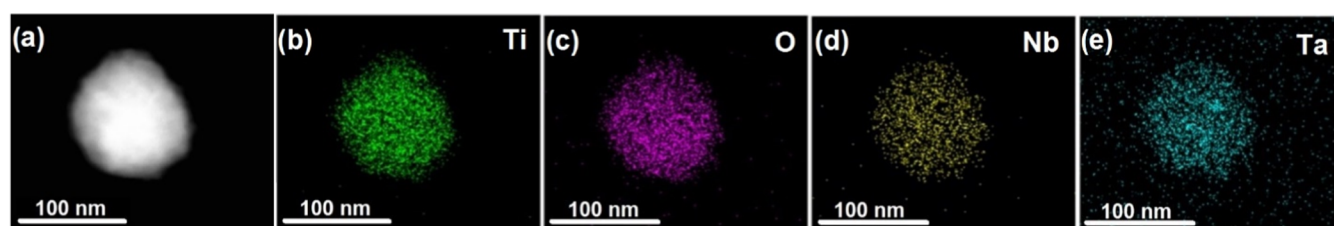


Figure 3. (a) STEM image of a NTTO nanoparticle and its STEM-EDX elemental maps for (b–e) titanium, oxygen, niobium, and tantalum.

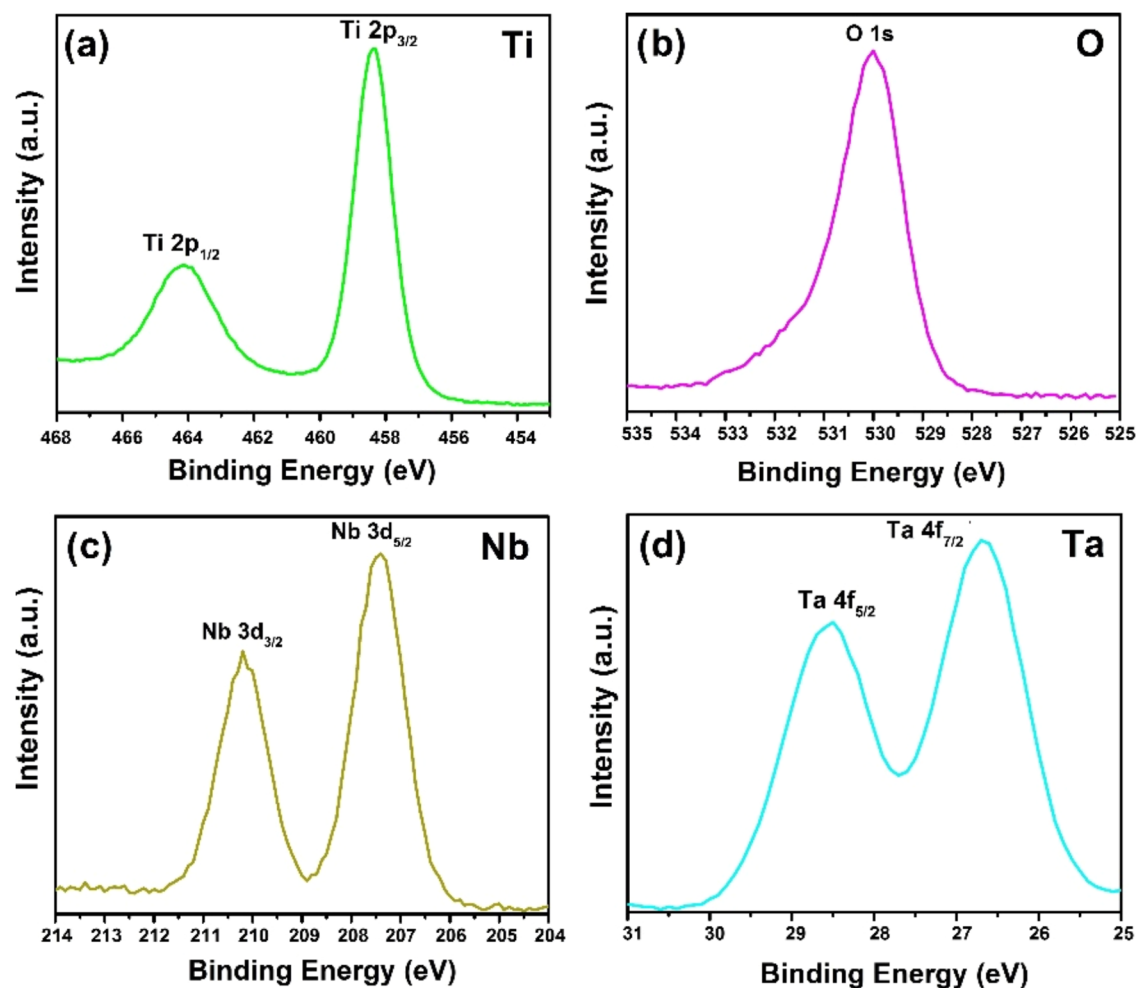
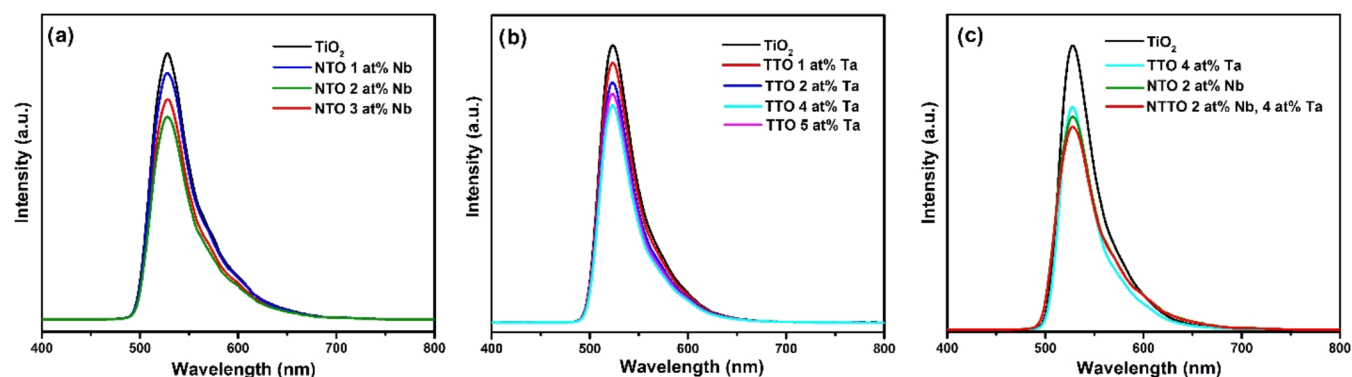


Figure 4. X-ray photoelectron spectra for (a) titanium, (b) oxygen, (c) niobium, and (d) tantalum in NTTO nanoparticles.

of the doped nanoparticles were determined by energy-dispersive X-ray spectroscopy in conjunction with a scanning transmission electron microscope (STEM-EDX). The STEM-EDX spectra of all doped nanoparticles exhibited characteristic peaks for titanium (Ti  $K\alpha$  and Ti  $L\alpha$ ) at 4.508 keV and 0.452 keV, respectively, along with oxygen (O  $K\alpha$ ) peak at 0.525 keV as shown in Figure S2–4. For NTO nanoparticles, the niobium (Nb  $K\alpha$  and Nb  $L\alpha$ ) peaks were detected at 16.581 keV and 2.166 keV, respectively (Figure S2). Tantalum (Ta  $K\alpha$  and Ta  $M$ ) peaks at 8.145 keV (this peak appeared as the shoulder to the more prominent Cu  $K\alpha$  at 8.041 keV) and 1.709 keV were identified in the TTO nanoparticle spectrum (Figure S3). In the NTTO nanoparticles, the characteristic peaks for both niobium (Ta  $K\alpha$  and Ta  $L\alpha$ ) and tantalum (Ta  $K\alpha$  and Ta  $M$ ) were all present at their respective energies, as shown in Figure S4. Additionally, peaks corresponding to copper (Cu  $K\alpha$  and

Cu  $L\alpha$ ) at 8.041 keV and 0.931 keV, and a prominent carbon (C  $K\alpha$ ) peak at 0.278 keV, were also observed, which can be attributed to the copper grid on carbon films used for sample preparation in the STEM-EDX analysis.

The STEM-EDX elemental mapping was conducted for NTTO (Figure 3a–e), NTO (Figure S5), and TTO (Figure S6) nanoparticles to evaluate the dopant distributions within the doped TiO<sub>2</sub> structures. These elemental maps confirmed the successful and uniform incorporation of Nb and Ta dopants into the TiO<sub>2</sub> nanoparticles. Notably, the atomic concentrations of NTTO nanoparticles closely matched those in the singly doped NTO and TTO nanoparticles (Table S5). This finding highlights the effectiveness of our synthetic process in controlling dopant compositions, even for the dually doped NTTO nanoparticles. Such consistent and uniform doping results require thorough premixing of TBOT with



**Figure 5.** Photoluminescence spectra of (a) NTO, (b) TTO nanoparticles at various dopant concentrations, and (c) NTTO nanoparticles at 2 atom % Nb/4 atom % Ta.

$\text{Nb}(\text{OEt})_5$ , and  $\text{Ta}(\text{OEt})_5$  in the same solution before introducing it to the preheated ethanol/Lutensol ON 70 mixture. This preparatory step is crucial for achieving reliable doping outcomes.

**X-ray Photoelectron Spectroscopy Analysis of Doped  $\text{TiO}_2$  Nanoparticles.** To complement the study on dopant characteristics, X-ray photoelectron spectroscopy (XPS) was employed to confirm the incorporation of Nb and Ta into the  $\text{TiO}_2$  lattice. The XPS results for NTTO (Figure 4a–d), NTO (Figure S7), and TTO (Figure S8) nanoparticles revealed O 1s peaks at  $\sim 530$  eV, indicative of oxygen, as well as Ti  $2p_{3/2}$  and Ti  $2p_{1/2}$  peaks at  $\sim 458.5$  and  $\sim 464.3$  eV, respectively, confirming the presence of titanium. The Nb  $3d_{5/2}$  and Nb  $3d_{3/2}$  peaks observed at 207.4 and 210.1 eV, respectively, verify the inclusion of Nb into the  $\text{TiO}_2$  lattice. Similarly, the presence of Ta was confirmed by Ta  $4f_{7/2}$  and Ta  $4f_{5/2}$  peaks, which were detected at their characteristic binding energies of 26.7 and 28.5 eV, respectively.

The atomic concentrations for dopant elements were calculated for all samples of doped  $\text{TiO}_2$  nanoparticles. The results showed high consistency with the data obtained from EDX not only for NTO and TTO but also for NTTO nanoparticles, as shown in Table S5. This consistency indicates that the dopant atoms were uniformly incorporated throughout the nanoparticles. Significantly, such verification ensures a predictable relationship between the elemental ratios in the starting materials and the elemental compositions of the synthesized nanoparticles. This predictability is crucial for tailoring the nanoparticles to achieve desired properties, which will be further discussed below.

**Photoluminescence Spectra of Doped  $\text{TiO}_2$  Nanoparticles.** In semiconductor nanomaterials, the recombination of electron–hole pairs is a critical factor influencing their photocatalytic activity.<sup>9</sup> The energy emitted during this recombination process can be captured by photoluminescence (PL) spectroscopy, where the signal intensity serves as an indicator of the electron–hole recombination rate within the semiconductor nanostructure.<sup>9</sup> To ensure a consistent and accurate assessment of doping effects on the electron–hole recombination rate, the PL spectra of the nanoparticles were normalized based on particle concentration and volume. The observed PL peak at  $\sim 525$  nm aligns with previous studies on  $\text{TiO}_2$  photoluminescence.<sup>51–53</sup> We noted a trend where PL signal intensities decreased with increasing doping concentrations, reaching minimum intensities at doping thresholds of 2 atom % for Nb and 4 atom % for Ta (Figure 5a–b). Interestingly, beyond these thresholds, such as at 3 atom % Nb,

the PL signal intensity increased again. These findings suggest a direct correlation between the doping concentrations and electron–hole recombination rates in  $\text{TiO}_2$ , likely due to a decrease in oxygen vacancies and defects in the host material upon doping,<sup>54</sup> which could significantly impact its photocatalytic efficiency.

For NTO nanoparticles, it was observed that the PL signal decreased proportionally with increasing Nb concentration, achieving a 25% reduction in signal intensity at the 2 atom % Nb threshold as shown in Figure 5a and Table S6. However, upon increasing the doping level to 3 atom % Nb, the PL signal reduction decreased to 14%, suggesting a reversal in the trend. This change might be due to the formation of a different phase<sup>55</sup> with a higher electron–hole recombination rate or the creation of new recombination centers,<sup>56</sup> induced by excess doping levels. A similar pattern was noted for TTO nanoparticles, where the maximum PL signal reduction of 22% occurred at 4 atom % Ta doping, as shown in Figure 5b and Table S6. These reductions in electron–hole recombination rates through Nb and Ta doping make NTO and TTO nanoparticles more promising for various photocatalytic and optoelectronic applications. Based on the identified doping thresholds of 2 atom % Nb and 4 atom % Ta, the synthesis conditions for NTTO nanoparticles were optimized to explore the combined effects of Nb and Ta doping on  $\text{TiO}_2$  nanoparticles. Remarkably, the NTTO nanoparticles codoped with 2 atom % Nb and 4 atom % Ta exhibited a higher reduction in the electron–hole recombination rate, with a 30% reduction in the PL signal intensity compared to 25% for NTO with 2 atom % Nb and 22% for TTO with 4 atom % Ta, respectively (Figure 5c and Table S6). This synergistic effect of multiple dopants has been observed in other material systems as well,<sup>57,58</sup> suggesting that the incorporation of multiple elements with different atomic radii could introduce additional lattice stress in the host  $\text{TiO}_2$  material, potentially leading to more defects. This hypothesis is supported by the notably smaller crystallite sizes of NTTO observed in XRD analysis, which could prolong the electron–hole recombination process. As shown in Table S4, the incorporation of Ta and Nb dopants into the  $\text{TiO}_2$  lattice led to a reduction in average crystallite size. Despite maintaining the same overall particle size, the smaller crystallites might have caused the photogenerated electrons and holes to travel and scatter through an increased number of crystallite interfaces. This effect likely reduced their probability of recombination, leading to the observed decrease in the PL signal. Interestingly, the correlation between smaller crystallite sizes and the reduction of electron–hole recombi-

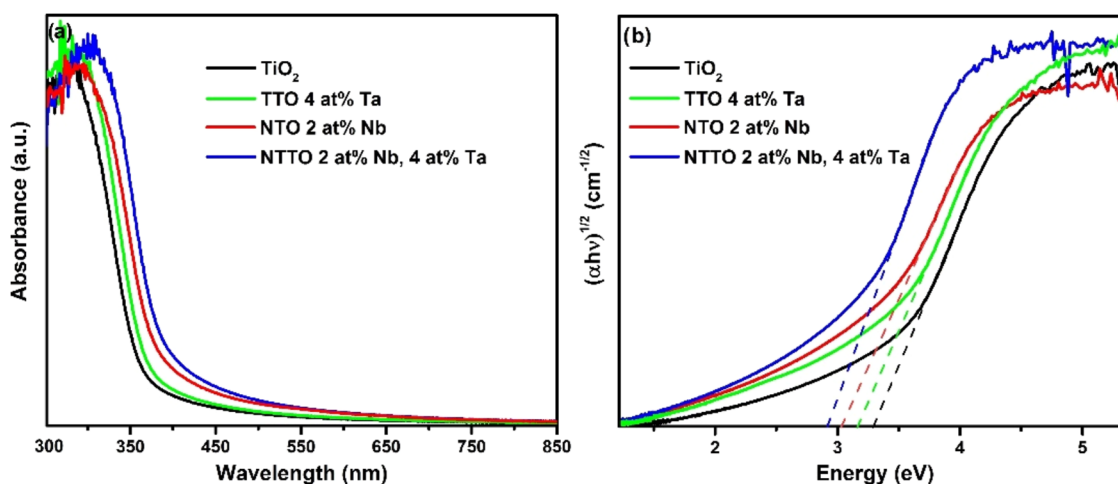


**Figure 6.** (a) Solid-state diffuse reflectance spectra and (b) Tauc plot of TiO<sub>2</sub>, TTO with 4 atom % Ta, NTO with 2 atom % Nb, and NTTO with 2 atom % Nb/4 atom % Ta nanoparticles.

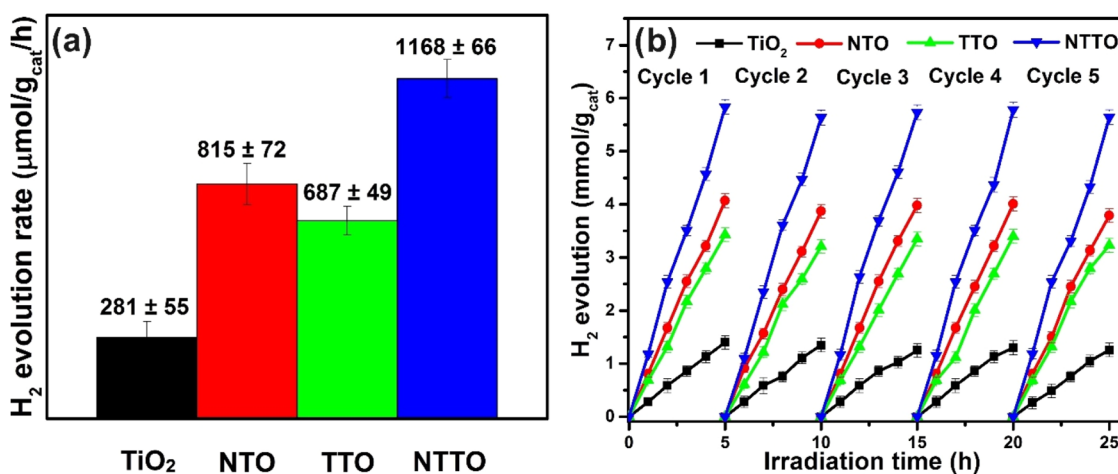


**Figure 7.** (a) Hydrogen evolution rates of TiO<sub>2</sub>, NTO, TTO, and NTTO nanoparticles and (b) their cyclability in photocatalytic hydrogen evolution.

nation processes were consistently observed in various types of semiconducting materials, such as TiO<sub>2</sub>,<sup>59</sup> perovskite,<sup>60</sup> and BiVO<sub>4</sub>.<sup>61</sup> The capability to modulate the PL signal through controlled dopant concentrations using the facile synthetic method further expands the utility of NTO, TTO, and NTTO nanoparticles for advanced applications. With their optimized electron–hole recombination rates, NTO (2 atom % Nb), TTO (4 atom % Ta), and NTTO (2 atom % Nb and 4 atom % Ta) nanoparticles will be subjected to further studies to evaluate their optical properties and photocatalytic hydrogen evolution performance in subsequent sections of this report.

#### Band Gap Analyses for Doped TiO<sub>2</sub> Nanoparticles.

The optical band gaps ( $E_g$ ) of undoped, singly doped, and dually doped TiO<sub>2</sub> nanoparticles were determined using diffuse reflectance spectroscopy (DRS) absorbance measurements, applying the Tauc eq (eq 1) for indirect band gap materials,<sup>62</sup> with  $r = 2$ , where  $r$  represents the power factor in the equation,  $\alpha$  is the absorption coefficient,  $h\nu$  denotes the incident photon energy,  $E_g$  is the optical band gap, and  $A$  is a proportional constant. The equation is as follows

$$\alpha h\nu = A(h\nu - E_g)^r \quad (1)$$

Solid-state DRS measurements were conducted on dried nanoparticles to obtain the absorption spectra across the UV–vis–NIR range. As illustrated in Figure 6a, the absorption spectra for TiO<sub>2</sub>, NTO, TTO, and NTTO nanoparticles showed slight shifts in the positions of absorption peaks for all doped samples, with the most pronounced shift observed in NTTO nanoparticles compared to undoped TiO<sub>2</sub> counterparts. For a more detailed analysis, Tauc plots of  $(\alpha h\nu)^{1/2}$  versus photon energy ( $h\nu$ ) were generated as shown in Figure 6b. These plots revealed shifts toward lower energy levels, aligning with the shifts toward longer wavelengths in the absorption spectra (Figure 6a), indicating changes in the optical band gaps with doping.

The optical band gap of anatase TiO<sub>2</sub> nanoparticles was found to be 3.27 eV, which is slightly larger than bulk anatase TiO<sub>2</sub>,<sup>63</sup> as anticipated due to the quantum confinement effect often observed in nanoscale semiconductors. The introduction of Nb and Ta dopants into TiO<sub>2</sub> nanoparticles resulted in a decrease in the optical band gaps to 3.15 eV for TTO, 3.02 eV for NTO, and 2.90 eV for NTTO, respectively (Figure 6b). This reduction in the optical band gap can be attributed to the inclusion of dopants introducing either donor or acceptor levels in the band gap region of the metal oxide semiconductors, effectively narrowing the band gap.<sup>64</sup> Interestingly,

**Table 1. Optical Band Gaps, Hydrogen Evolution Rates, and Apparent Quantum Yields of TiO<sub>2</sub>, NTO, TTO, and NTTO Nanoparticles**

	TiO <sub>2</sub>	NTO	TTO	NTTO
band gap (eV)	3.27 ± 0.02	3.02 ± 0.03	3.15 ± 0.02	2.90 ± 0.02
H <sub>2</sub> evolution rate (μmol/g <sub>cat</sub> /h)	281 ± 55	815 ± 72	687 ± 49	1168 ± 66
AQY <sup>a</sup> (%)	2.18 ± 0.23	4.28 ± 0.26	3.69 ± 0.28	6.74 ± 0.31

<sup>a</sup>AQY calculated at 365 nm.

the simultaneous doping of Nb and Ta into the TiO<sub>2</sub> lattice led to a further reduction in the band gap energy of the NTTO nanoparticles, enhancing their efficiency in harvesting the center part of the solar spectrum. As shown in Figure 6b, the dopant elements influenced the Tauc plot to shift toward lower energies, which in turn extended the absorption tails of the nanoparticles (Figure 6a). The observed effects of dopants on the optical properties (photoluminescence, band gap) in our doped TiO<sub>2</sub> system have been reported in other doped TiO<sub>2</sub> system,<sup>11</sup> reinforcing the validity of our study while providing new insights into the synergistic effects of a dual-doping system.

**Photocatalytic Hydrogen Evolution.** The photocatalytic performance of undoped, singly doped, and dually doped TiO<sub>2</sub> nanoparticles for hydrogen evolution reaction (HER) was evaluated in a basic environment at 25 °C under a simulated solar illumination. The commonly used test medium for hydrogen evolution, consisting of a 10% aqueous solution of ethylene glycol, is employed, with ethylene glycol serving as the sacrificial agent. Gas chromatography confirmed the hydrogen gas production, with the results presented in Figure S9. The amounts of hydrogen produced over time by TiO<sub>2</sub>, NTO, TTO, and NTTO nanoparticles are shown in Figure 7a, demonstrating that the hydrogen evolution rates for these samples remained consistent for at least 5 h. The hydrogen evolution rate for undoped anatase TiO<sub>2</sub> was ~281 μmol/g<sub>cat</sub>/h, and doping enhanced this rate to ~687 μmol/g<sub>cat</sub>/h for TTO, ~815 μmol/g<sub>cat</sub>/h for NTO, and ~1168 μmol/g<sub>cat</sub>/h for NTTO, respectively (Figure 7b). Hence, compared to undoped TiO<sub>2</sub>, the photocatalytic hydrogen evolution rates for TTO and NTO nanoparticles increased by ~2.4, ~2.9 times, respectively. Notably, the dually doped NTTO nanoparticles showed a hydrogen evolution rate ~4.2 times higher than that of undoped TiO<sub>2</sub>, indicating a substantial improvement. This rate was also 70 and 43% higher than those for TTO and NTO nanoparticles, respectively. These enhancements can be attributed to a synergistic effect arising from the reduced band gap energies, facilitating greater photon absorption at wavelengths closer to the center of solar spectrum, coupled with the decreased electron–hole recombination rates observed in the doped nanoparticles. We note also the possible contribution of crystallite size, where the data in Table S4 and Figure 7 show a correlation between small crystallite size and hydrogen evolution. However, the introduction of dopants is highlighted as the most significant factor. The incorporation of Ta and Nb dopants creates multiple donor energy levels below the conduction band of pristine TiO<sub>2</sub>, significantly facilitating electron transitions from the valence band to the conduction band.<sup>65–67</sup> This results in a higher generation rate of charge carriers and an enhanced hydrogen evolution reaction.

The apparent quantum yields (AQYs) for each nanoparticle sample tested in the photocatalytic hydrogen evolution were also calculated at 365 nm for all four testing nanoparticles.

Details about AQY calculation can be found in the Supporting Information. With enhanced hydrogen evolution rates by the presence of the dopants, the AQYs of TTO, NTO, and NTTO were significantly increased to ~3.69, ~4.28, and ~6.74%, respectively, from ~2.18% of pristine anatase TiO<sub>2</sub> as shown in Table 1. Thus, these results pinpointed that the doped nanoparticles were able to utilize the incident photons more effectively for hydrogen generation than the undoped TiO<sub>2</sub> nanoparticles.

Cyclability tests were also carried out on the same nanoparticle samples to evaluate their photocatalytic stabilities. Specifically, the nanoparticles were collected, washed, and reused after each photocatalytic hydrogen evolution test. Notably, all the nanoparticles remained highly stable after five test cycles, as shown in Figure 7b. The results showed almost no change in hydrogen evolution performance, indicating that the nanoparticles did not undergo significant alterations as a result of the catalytic reaction. The minor variations of the evolved hydrogen fell within experimental and instrumental errors (e.g., the testing process involved several transferring steps, which might have slightly reduced the actual amount of nanoparticle catalyst in each subsequent cycle). Thus, both the optical property analyses and hydrogen evolution studies have demonstrated significant enhancements in the Nb-, Ta-, and especially the Nb/Ta codoped TiO<sub>2</sub> nanoparticles, enabling them for scale-up applications in photocatalytic hydrogen generation. Moreover, the applicability prospect of the doped TiO<sub>2</sub> can even be further boosted by hybridizing with suitable plasmonic nanostructures.<sup>68</sup>

Finally, it is worth noting that the TiO<sub>2</sub> photocatalysts in our study demonstrated superior hydrogen evolution performance without requiring cocatalysts to enhance the kinetics of redox reactions or facilitate electron transfer. The best performance was achieved by our uniquely dually doped titanate nanoparticles, NTTO, with a hydrogen evolution rate of 1168 μmol/g/h. We envision that our work is the first to report highly uniform singly and dually doped TiO<sub>2</sub> nanoparticles for HER. Therefore, comparisons with other studies on Ta- and Nb-doped TiO<sub>2</sub>, which exhibit varying levels of nanoparticle quality, are arguably irrelevant. Consequently, no direct comparison with other similar doped TiO<sub>2</sub> nanoparticles for HER will be made here. Recently reported TiO<sub>2</sub>-based nanostructured catalysts, supported by cocatalysts such as α-MoS<sub>2</sub>/TiO<sub>2</sub> or heterojunction structures such as TiO<sub>2</sub>@g-C<sub>3</sub>N<sub>4</sub>, exhibited lower hydrogen evolution rates.<sup>69,70</sup> These observations suggest that further loading of efficient cocatalysts onto our highly uniform NTTO nanoparticles could further enhance their performance, potentially achieving competitive photocatalytic efficiency. These findings point to a promising pathway for future research in designing high-performance hydrogen evolution catalysts.

## CONCLUSIONS

This work demonstrates a reliable and convenient wet chemistry approach for synthesizing highly monodisperse undoped, singly, and dually doped anatase TiO<sub>2</sub> nanoparticles with Nb and/or Ta as dopants. The introduction of Nb and Ta dopants effectively suppressed electron–hole recombination rates. Singly doped nanoparticles showed optimal recombination suppression at doping levels of 2 atom % Nb and 4 atom % Ta, leading to PL signal reduction of 25 and 22%, respectively. In dually doped nanoparticles, a further reduction to 30% was observed with codoping of Nb (2 atom %) and Ta (4 atom %). The optical band gap of undoped TiO<sub>2</sub> nanoparticles, at 3.27 eV, was significantly narrowed to 3.15 eV for TTO and 3.02 eV for NTO, with the most substantial reduction observed in NTTTO nanoparticles at 2.90 eV. Importantly, photocatalytic hydrogen evolution tests revealed enhanced hydrogen evolution rates, which are 2.4 times (TTO), 2.9 times (NTO), and 4.2 times (NTTO) higher than that of undoped TiO<sub>2</sub> nanoparticles. Moreover, all nanoparticle variants maintained high stability after multiple photocatalytic hydrogen evolution test cycles. The notable improvements in hydrogen evolution rates, particularly for the dually doped nanoparticles, along with the scalability and mild conditions used in the synthetic methods, render these doped TiO<sub>2</sub> nanoparticles promising for fuel generation and other photocatalytic applications. Additionally, their tunable PL responses and optical band gaps extend their potential to optoelectronics and gas sensing applications.

## ASSOCIATED CONTENT

### Supporting Information

The Supporting Information is available free of charge at <https://pubs.acs.org/doi/10.1021/acsanm.5c00391>.

SEM images and size distributions of NTO, TTO, NTTTO nanoparticles (Figure S1); Reaction conditions used for the syntheses (Table S1) as well as the average DLS size and  $\zeta$  potential (Table S2) of TiO<sub>2</sub>, NTO, TTO, and NTTTO nanoparticles; XRD peak positions and reference indices of corresponding crystallographic planes (Table S3) and crystallite sizes (Table S4) of the undoped and doped TiO<sub>2</sub> nanoparticles; dopant concentrations measured by XPS and EDX (Table S5) and photoluminescence signal reduction of doped nanoparticles (Table S6); STEM-EDX spectra of NTO (Figure S2), TTO (Figure S3), NTTTO (Figure S4) nanoparticles; STEM-EDX elemental maps of NTO (Figure S5) and TTO (Figure S6) nanoparticles; XPS spectra of NTO (Figure S7), TTO (Figure S8) nanoparticles; apparent quantum yield (AQY) calculations; gas chromatography measurements of photocatalytic hydrogen evolution gas product as compared with pure hydrogen calibration (Figure S9) (PDF)

## AUTHOR INFORMATION

### Corresponding Author

T. Randall Lee – Department of Chemistry and the Texas Center for Superconductivity, University of Houston, Houston, Texas 77204-5003, United States; [orcid.org/0000-0001-9584-8861](https://orcid.org/0000-0001-9584-8861); Email: [trlee@uh.edu](mailto:trlee@uh.edu)

## Authors

Nhat M. Ngo – Department of Chemistry and the Texas Center for Superconductivity, University of Houston, Houston, Texas 77204-5003, United States

Minh Dang Nguyen – Department of Chemistry and the Texas Center for Superconductivity, University of Houston, Houston, Texas 77204-5003, United States; [orcid.org/0000-0002-2569-8279](https://orcid.org/0000-0002-2569-8279)

Hung-Vu Tran – Department of Chemistry and the Texas Center for Superconductivity, University of Houston, Houston, Texas 77204-5003, United States; NTT Hi-Tech Institute, Nguyen Tat Thanh University, Ho Chi Minh City 7280, Vietnam; [orcid.org/0000-0001-8536-2737](https://orcid.org/0000-0001-8536-2737)

Riddhiman Medhi – Department of Chemistry, University of Scranton, Scranton, Pennsylvania 18510, United States; [orcid.org/0000-0002-2368-2468](https://orcid.org/0000-0002-2368-2468)

Jong Moon Lee – Department of Chemistry and the Texas Center for Superconductivity, University of Houston, Houston, Texas 77204-5003, United States

Complete contact information is available at: <https://pubs.acs.org/doi/10.1021/acsanm.5c00391>

## Notes

The authors declare no competing financial interest.

## ACKNOWLEDGMENTS

The authors are grateful for financial support from the Air Force Office of Scientific Research (FA9550-23-1-0581; 23RT0567) and the Robert A. Welch Foundation (Grant Nos. E-1320 and V-E-0001).

## REFERENCES

- Wang, Q.; Domen, K. Particulate Photocatalysts for Light-Driven Water Splitting: Mechanisms, Challenges, and Design Strategies. *Chem. Rev.* **2020**, *120*, 919–985.
- Fujishima, A.; Honda, K. Electrochemical Photolysis of Water at a Semiconductor Electrode. *Nature* **1972**, *238*, 37–38.
- Li, J.; Su, W.; Li, J.; Wang, L.; Ren, J.; Zhang, S.; Cheng, P.; Hong, H.; Wang, D.; Zhou, Y.; Mi, W.; Du, Y. Orientational Alignment of Oxygen Vacancies: Electric-Field-Inducing Conductive Channels in TiO<sub>2</sub> Film to Boost Photocatalytic Conversion of CO<sub>2</sub> into CO. *Nano Lett.* **2021**, *21*, 5060–5067.
- Jayachitra, S.; Natarajan Pugazhendhi, K.; Kumaravel, D. K.; Murugan, P.; Sathish, M. Supercritical Fluid-Assisted Synthesis of Metal Selenide/TiO<sub>2</sub> Nanocomposites for Photocatalytic Hydrogen Production. *ACS Appl. Nano Mater.* **2024**, *7*, 4853–4864, DOI: [10.1021/acsanm.3c05585](https://doi.org/10.1021/acsanm.3c05585).
- Yu, F.; Wang, X.; Lu, H.; Li, G.; Liao, B.; Wang, H.; Duan, C.; Mao, Y.; Chen, L. Surface Engineering of TiO<sub>2</sub> Nanosheets to Boost Photocatalytic Methanol Dehydrogenation for Hydrogen Evolution. *Inorg. Chem.* **2023**, *62*, 5700–5706.
- Plaça, L. F.; Vital, P.-L. S.; Gomes, L. E.; Roveda, A. C.; Cardoso, D. R.; Martins, C. A.; Wender, H. Black TiO<sub>2</sub> Photoanodes for Direct Methanol Photo Fuel Cells. *ACS Appl. Mater. Interfaces* **2023**, *15*, 43259–43271.
- Krivtsov, I.; Ilkaeva, M.; Avdin, V.; Amghouz, Z.; Khainakov, S. A.; García, J. R.; Díaz, E.; Ordóñez, S. Exceptional Thermal Stability of Undoped Anatase TiO<sub>2</sub> Photocatalysts Prepared by a Solvent-Exchange Method. *RSC Adv.* **2015**, *5*, 36634–36641.
- Grande, F.; Tucci, P. Titanium Dioxide Nanoparticles: A Risk for Human Health? *Mini-Rev. Med. Chem.* **2016**, *16*, 762–769.
- Ma, Y.; Wang, X.; Jia, Y.; Chen, X.; Han, H.; Li, C. Titanium Dioxide-Based Nanomaterials for Photocatalytic Fuel Generations. *Chem. Rev.* **2014**, *114*, 9987–10043.

- (10) Mistry, H.; Varela, A. S.; Kühl, S.; Strasser, P.; Cuenya, B. R. Nanostructured Electro catalysts with Tunable Activity and Selectivity. *Nat. Rev. Mater.* **2016**, *1*, No. 16009.
- (11) Medhi, R.; Marquez, M. D.; Lee, T. R. Visible-Light-Active Doped Metal Oxide Nanoparticles: Review of Their Synthesis, Properties, and Applications. *ACS Appl. Nano Mater.* **2020**, *3*, 6156–6185.
- (12) Li, Y.; Peng, Y.-K.; Hu, L.; Zheng, J.; Prabhakaran, D.; Wu, S.; Puchtl, T. J.; Li, M.; Wong, K.-Y.; Taylor, R. A.; Tsang, S. C. E. Photocatalytic Water Splitting by N-TiO<sub>2</sub> on MgO (111) with Exceptional Quantum Efficiencies at Elevated Temperatures. *Nat. Commun.* **2019**, *10*, No. 4421.
- (13) Usui, H.; Domi, Y.; Yamamoto, Y.; Hoshi, T.; Tanaka, T.; Oishi, N.; Nitta, N.; Sakaguchi, H. Nickel-Doped Titanium Oxide with Layered Rock-Salt Structure for Advanced Li-Storage Materials. *ACS Appl. Electron. Mater.* **2023**, *5*, 6292–6304.
- (14) Usui, H.; Domi, Y.; Nguyen, T. H.; Sadamori, Y.; Tanaka, T.; Sakaguchi, H. Fe–Nb Co-Doped Rutile TiO<sub>2</sub> for Anode Materials of Li-Ion Batteries. *ACS Appl. Eng. Mater.* **2023**, *1*, 994–1000.
- (15) Mei, W.; Lu, H.; Dong, R.; Tang, S.; Xu, J. Ce-Doped Brookite TiO<sub>2</sub> Quasi-Nanocubes for Efficient Visible Light Catalytic Degradation of Tetracycline. *ACS Appl. Nano Mater.* **2024**, *7*, 1825–1834.
- (16) Culu, A.; Kaya, I. C.; Sonmezoglu, S. Spray-Pyrolyzed Tantalum-Doped TiO<sub>2</sub> Compact Electron Transport Layer for UV-Photostable Planar Perovskite Solar Cells Exceeding 20% Efficiency. *ACS Appl. Energy Mater.* **2022**, *5*, 3454–3462.
- (17) Cao, S.; Zhang, S.; Zhang, T.; Lee, J. Y. Fluoride-Assisted Synthesis of Plasmonic Colloidal Ta-Doped TiO<sub>2</sub> Nanocrystals for Near-Infrared and Visible-Light Selective Electrochromic Modulation. *Chem. Mater.* **2018**, *30*, 4838–4846.
- (18) Acchutharaman, K. R.; Santhosh, N.; Senthil Pandian, M.; Ramasamy, P. Improved Optoelectronic Properties of Rutile TiO<sub>2</sub> Nanorods through Strontium Doping for the Economical and Efficient Perovskite Solar Cells. *Mater. Res. Bull.* **2023**, *160*, No. 112141.
- (19) Rajaramanan, T.; Shanmugaratnam, S.; Gurunanthan, V.; Yohi, S.; Velauthapillai, D.; Ravirajan, P.; Senthilnathan, M. Cost Effective Solvothermal Method to Synthesize Zn-Doped TiO<sub>2</sub> Nanomaterials for Photovoltaic and Photocatalytic Degradation Applications. *Catalysts* **2021**, *11*, 690.
- (20) Sun, W.; Dong, X.; Huang, P.; Shan, J.; Qi, L.; Zhou, J. Solvothermal Synthesis of Nb-Doped TiO<sub>2</sub> Nanoparticles with Enhanced Sonodynamic Effects for Destroying Tumors. *RSC Adv.* **2021**, *11*, 36920–36927.
- (21) Mugundan, S.; Praveen, P.; Sridhar, S.; Prabu, S.; Lawrence Mary, K.; Ubaidullah, M.; Shaikh, S. F.; Kanagesan, S. Sol-Gel Synthesized Barium Doped TiO<sub>2</sub> Nanoparticles for Solar Photocatalytic Application. *Inorg. Chem. Commun.* **2022**, *139*, No. 109340.
- (22) Bhosale, M. G.; Sutar, R. S.; Deshmukh, S. B.; Patil, M. K. Photocatalytic Efficiency of Sol–Gel Synthesized Mn-doped TiO<sub>2</sub> Nanoparticles for Degradation of Brilliant Green Dye and Mixture of Dyes. *J. Chin. Chem. Soc.* **2022**, *69*, 1730–1743.
- (23) Fazil, M.; Alshehri, S. M.; Mao, Y.; Ahmad, T. Enhanced Photo/Electrocatalytic Hydrogen Evolution by Hydrothermally Derived Cu-Doped TiO<sub>2</sub> Solid Solution Nanostructures. *Langmuir* **2024**, *40*, 4063–4076, DOI: 10.1021/acs.langmuir.3c02860.
- (24) Liu, B.; Chen, H. M.; Liu, C.; Andrews, S. C.; Hahn, C.; Yang, P. Large-Scale Synthesis of Transition-Metal-Doped TiO<sub>2</sub> Nanowires with Controllable Overpotential. *J. Am. Chem. Soc.* **2013**, *135*, 9995–9998.
- (25) Lawrence, M. J.; Celorrio, V.; Shi, X.; Wang, Q.; Yanson, A.; Adkins, N. J. E.; Gu, M.; Rodriguez-López, J.; Rodriguez, P. Electrochemical Synthesis of Nanostructured Metal-Doped Titanates and Investigation of Their Activity as Oxygen Evolution Photoanodes. *ACS Appl. Energy Mater.* **2018**, *1*, S233–S244.
- (26) Dorow-Gerspach, D.; Mergel, D.; Wuttig, M. Effects of Different Amounts of Nb Doping on Electrical, Optical and Structural Properties in Sputtered TiO<sub>2-x</sub> Films. *Crystals* **2021**, *11*, 301.
- (27) Yue, J.; Suchomski, C.; Voepel, P.; Ellinghaus, R.; Rohnke, M.; Leichtweiss, T.; Elm, M. T.; Smarsly, B. M. Mesoporous Niobium-Doped Titanium Dioxide Films from the Assembly of Crystalline Nanoparticles: Study on the Relationship between the Band Structure, Conductivity and Charge Storage Mechanism. *J. Mater. Chem. A* **2017**, *5*, 1978–1988.
- (28) Ribeiro, J. M.; Correia, F. C.; Rodrigues, F. J.; Reparaz, J. S.; Goñi, A. R.; Tavares, C. J. Transparent Niobium-Doped Titanium Dioxide Thin Films with High Seebeck Coefficient for Thermoelectric Applications. *Surf. Coat. Technol.* **2021**, *425*, No. 127724.
- (29) Singh, S.; Sharma, V.; Sachdev, K. Investigation of Effect of Doping Concentration in Nb-Doped TiO<sub>2</sub> Thin Films for TCO Applications. *J. Mater. Sci.* **2017**, *52*, 11580–11591.
- (30) Nikodemski, S.; Dameron, A. A.; Perkins, J. D.; O’Hayre, R. P.; Ginley, D. S.; Berry, J. J. The Role of Nanoscale Seed Layers on the Enhanced Performance of Niobium Doped TiO<sub>2</sub> Thin Films on Glass. *Sci. Rep.* **2016**, *6*, No. 32830.
- (31) Saha, D.; Selvaganapathy, P. R.; Kruse, P. Peroxide-Induced Tuning of the Conductivity of Nanometer-Thick MoS<sub>2</sub> Films for Solid-State Sensors. *ACS Appl. Nano Mater.* **2020**, *3*, 10864–10877.
- (32) Singkammo, S.; Wisitsoraat, A.; Sriprachubwong, C.; Tuantranont, A.; Phanichphant, S.; Liewhiran, C. Electrolytically Exfoliated Graphene-Loaded Flame-Made Ni-Doped SnO<sub>2</sub> Composite Film for Acetone Sensing. *ACS Appl. Mater. Interfaces* **2015**, *7*, 3077–3092.
- (33) Lü, X.; Yang, W.; Quan, Z.; Lin, T.; Bai, L.; Wang, L.; Huang, F.; Zhao, Y. Enhanced Electron Transport in Nb-Doped TiO<sub>2</sub> Nanoparticles via Pressure-Induced Phase Transitions. *J. Am. Chem. Soc.* **2014**, *136*, 419–426.
- (34) Su, H.; Huang, Y.-T.; Chang, Y.-H.; Zhai, P.; Hau, N. Y.; Cheung, P. C. H.; Yeh, W.-T.; Wei, T.-C.; Feng, S.-P. The Synthesis of Nb-Doped TiO<sub>2</sub> Nanoparticles for Improved-Performance Dye Sensitized Solar Cells. *Electrochim. Acta* **2015**, *182*, 230–237.
- (35) Štengl, V.; Houšková, V.; Bakardjieva, S.; Murafa, N.; Bezdička, P. Niobium and Tantalum Doped Titania Particles. *J. Mater. Res.* **2010**, *25*, 2015–2024.
- (36) Kumar, A.; Ramani, V. Strong Metal–Support Interactions Enhance the Activity and Durability of Platinum Supported on Tantalum-Modified Titanium Dioxide Electrocatalysts. *ACS Catal.* **2014**, *4*, 1516–1525.
- (37) Liu, Y.; Pan, X.; Chen, W.; Zhao, X. Titanate-Derived Nb-Doped TiO<sub>2</sub> Nanoparticles Displaying Improved Lithium Storage Performance. *Dalton Trans.* **2022**, *51*, 2506–2511.
- (38) Le, N. T. H.; Thanh, T. D.; Pham, V.-T.; Phan, T. L.; Lam, V. D.; Manh, D. H.; Anh, T. X.; Le, T. K. C.; Thammajak, N.; Hong, L. V.; Yu, S. C. Structure and High Photocatalytic Activity of (N, Ta)-Doped TiO<sub>2</sub> Nanoparticles. *J. Appl. Phys.* **2016**, *120*, No. 142110.
- (39) Paul, R.; K, K.; S, P. Tantalum Doped Titanium Dioxide Nanoparticles for Efficient Photocatalytic Degradation of Dyes. *J. Mol. Struct.* **2023**, *1277*, No. 134869.
- (40) Mohamad Idris, N. H.; Cheong, K. Y.; Smith, S. M.; Lee, H. L. C,N-Codoped TiO<sub>2</sub> Nanoparticles Immobilized on Floating Alginate Beads for Diazinon Removal under Solar Light Irradiation. *ACS Appl. Nano Mater.* **2023**, *7*, 18273–18286.
- (41) Diego-Rucabado, A.; Merino-García, I.; Espeso, J. I.; González, J.; Arce, B.; Valiente, R.; Beobide, G.; Cano, I.; Martín-Rodríguez, R.; De Pedro, I.; Albo, J. Visible Light Active Ce-Doped and Cu–Ce Co-Doped TiO<sub>2</sub> Nanocrystals and Optofluidics for Clean Alcohol Production from CO<sub>2</sub>. *ACS Sustainable Chem. Eng.* **2023**, *11*, 13260–13273.
- (42) Dutta, S.; Patra, A. K.; De, S.; Bhaumik, A.; Saha, B. Self-Assembled TiO<sub>2</sub> Nanospheres By Using a Biopolymer as a Template and Its Optoelectronic Application. *ACS Appl. Mater. Interfaces* **2012**, *4*, 1560–1564.
- (43) Chiang, C.-H.; Kan, C.-W.; Wu, C.-G. Synergistic Engineering of Conduction Band, Conductivity, and Interface of Bilayered Electron Transport Layers with Scalable TiO<sub>2</sub> and SnO<sub>2</sub> Nanoparticles for High-Efficiency Stable Perovskite Solar Cells. *ACS Appl. Mater. Interfaces* **2021**, *13*, 23606–23615.

- (44) Chen, N.; Deng, D.; Li, Y.; Liu, X.; Xing, X.; Xiao, X.; Wang, Y. TiO<sub>2</sub> Nanoparticles Functionalized by Pd Nanoparticles for Gas-Sensing Application with Enhanced Butane Response Performances. *Sci. Rep.* **2017**, *7*, No. 7692.
- (45) Lim, C.; An, H.-R.; Ha, S.; Myeong, S.; Min, C. G.; Chung, H.-J.; Son, B.; Kim, C.-Y.; Park, J.-I.; Kim, H.; Lee, H. U.; Lee, Y.-S. Highly Visible-Light-Responsive Nanoporous Nitrogen-Doped TiO<sub>2</sub> (N-TiO<sub>2</sub>) Photocatalysts Produced by Underwater Plasma Technology for Environmental and Biomedical Applications. *Appl. Surf. Sci.* **2023**, *638*, No. 158123.
- (46) Ngo, N. M.; Omidian, M.; Tran, H.-V.; Lee, T. R. Stable Semi-Hollow Gold-Silver Nanostars with Tunable Plasmonic Resonances Ranging from Ultraviolet–Visible to Near-Infrared Wavelengths: Implications for Photocatalysis, Biosensing, and Theranostics. *ACS Appl. Nano Mater.* **2022**, *5*, 11391–11399.
- (47) Wang, F.; Richards, V. N.; Shields, S. P.; Buhro, W. E. Kinetics and Mechanisms of Aggregative Nanocrystal Growth. *Chem. Mater.* **2014**, *26*, 5–21.
- (48) Bryan, J. D.; Gamelin, D. R. Doped Semiconductor Nanocrystals: Synthesis, Characterization, Physical Properties, and Applications. In *Prog. Inorg. Chem.*; Karlin, K. D., Ed.; John Wiley & Sons, Inc.: Hoboken, NJ, 2005; pp 47–126 DOI: 10.1002/0471725560.ch2.
- (49) Azeez, F.; Al-Hetlani, E.; Arafa, M.; Abdelmonem, Y.; Nazeer, A. A.; Amin, M. O.; Madkour, M. The Effect of Surface Charge on Photocatalytic Degradation of Methylene Blue Dye Using Chargeable Titania Nanoparticles. *Sci. Rep.* **2018**, *8*, No. 7104.
- (50) Li, Y.; Qin, Z.; Guo, H.; Yang, H.; Zhang, G.; Ji, S.; Zeng, T. Low-Temperature Synthesis of Anatase TiO<sub>2</sub> Nanoparticles with Tunable Surface Charges for Enhancing Photocatalytic Activity. *PLoS One* **2014**, *9*, No. e114638.
- (51) Dozzi, M. V.; Candeo, A.; Marra, G.; D'Andrea, C.; Valentini, G.; Selli, E. Effects of Photodeposited Gold vs Platinum Nanoparticles on N,F-Doped TiO<sub>2</sub> Photoactivity: A Time-Resolved Photoluminescence Investigation. *J. Phys. Chem. C* **2018**, *122*, 14326–14335.
- (52) Ma, S.; Reish, M. E.; Zhang, Z.; Harrison, I.; Yates, J. T. Anatase-Selective Photoluminescence Spectroscopy of P25 TiO<sub>2</sub> Nanoparticles: Different Effects of Oxygen Adsorption on the Band Bending of Anatase. *J. Phys. Chem. C* **2017**, *121*, 1263–1271.
- (53) Pallotti, D. K.; Passoni, L.; Maddalena, P.; Di Fonzo, F.; Lettieri, S. Photoluminescence Mechanisms in Anatase and Rutile TiO<sub>2</sub>. *J. Phys. Chem. C* **2017**, *121*, 9011–9021.
- (54) Ni, Y.; Zhu, Y.; Ma, X. A Simple Solution Combustion Route for the Preparation of Metal-Doped TiO<sub>2</sub> Nanoparticles and Their Photocatalytic Degradation Properties. *Dalton Trans.* **2011**, *40*, 3689.
- (55) McCoy, J. J.; Swain, S. K.; Sieber, J. R.; Diercks, D. R.; Gorman, B. P.; Lynn, K. G. P-Type Doping Efficiency in CdTe: Influence of Second Phase Formation. *J. Appl. Phys.* **2018**, *123*, No. 161579.
- (56) Zhang, L.; Zheng, Q.; Xie, Y.; Lan, Z.; Prezhdo, O. V.; Saidi, W. A.; Zhao, J. Delocalized Impurity Phonon Induced Electron–Hole Recombination in Doped Semiconductors. *Nano Lett.* **2018**, *18*, 1592–1599.
- (57) Lee, W.; Oh, J.; Kwon, W.; Lee, S. H.; Kim, D.; Kim, S. Synthesis of Ag/Mn Co-Doped CdS/ZnS (Core/Shell) Nanocrystals with Controlled Dopant Concentration and Spatial Distribution and the Dynamics of Excitons and Energy Transfer between Co-Dopants. *Nano Lett.* **2019**, *19*, 308–317.
- (58) Sarfehjou, M.; Souri, D.; Khezripour, A. R. Functional Codoped ZnSe:Cu, Mn Quantum Dots(QDs): Microstructure, Calorimetric and Photoluminescence Properties. *Opt. Laser Technol.* **2022**, *145*, No. 107467.
- (59) Strauss, M.; Pastorello, M.; Sigoli, F. A.; Silva, J. M. de S. E.; Mazali, I. O. Singular Effect of Crystallite Size on the Charge Carrier Generation and Photocatalytic Activity of Nano-TiO<sub>2</sub>. *Appl. Surf. Sci.* **2014**, *319*, 151–157.
- (60) Kim, B. S.; Moon, G. H.; Park, S. C.; Jang, J.; Kang, Y. S. Effects of Crystal Size and Surface Coverage of Perovskites on Electron Recombination in Solar Cells. *Mater. Lett.* **2019**, *242*, 191–194.
- (61) Yabuta, M.; Takeda, A.; Sugimoto, T.; Watanabe, K.; Kudo, A.; Matsumoto, Y. Particle Size Dependence of Carrier Dynamics and Reactivity of Photocatalyst BiVO<sub>4</sub> Probed with Single-Particle Transient Absorption Microscopy. *J. Phys. Chem. C* **2017**, *121*, 22060–22066.
- (62) Zhu, T.; Gao, S.-P. The Stability, Electronic Structure, and Optical Property of TiO<sub>2</sub> Polymorphs. *J. Phys. Chem. C* **2014**, *118*, 11385–11396.
- (63) Luttrell, T.; Halpegamage, S.; Tao, J.; Kramer, A.; Sutter, E.; Batzill, M. Why Is Anatase a Better Photocatalyst than Rutile? - Model Studies on Epitaxial TiO<sub>2</sub> Films. *Sci. Rep.* **2014**, *4*, No. 4043.
- (64) Serpone, N. Is the Band Gap of Pristine TiO<sub>2</sub> Narrowed by Anion- and Cation-Doping of Titanium Dioxide in Second-Generation Photocatalysts? *J. Phys. Chem. B* **2006**, *110*, 24287–24293.
- (65) Ranjan, R.; Prakash, A.; Singh, A.; Singh, A.; Garg, A.; Gupta, R. K. Effect of Tantalum Doping in a TiO<sub>2</sub> Compact Layer on the Performance of Planar Spiro-OMeTAD Free Perovskite Solar Cells. *J. Mater. Chem. A* **2018**, *6*, 1037–1047.
- (66) Proch, S.; Kodama, K.; Yoshino, S.; Takahashi, N.; Kato, N.; Morimoto, Y. CO-Terminated Platinum Electrodeposition on Nb-Doped Bulk Rutile TiO<sub>2</sub>. *Electrocatalysis* **2016**, *7*, 362–375.
- (67) Aqeel, M.; Ikram, M.; Imran, M.; Ul-Hamid, A.; Qumar, U.; Shahbaz, A.; Ikram, M.; Saeed, A. TiO<sub>2</sub> Co-Doped with Zr and Ag Shows Highly Efficient Visible Light Photocatalytic Behavior Suitable for Treatment of Polluted Water. *RSC Adv.* **2020**, *10*, 42235–42248.
- (68) Kumar, A.; Choudhary, P.; Kumar, A.; Camargo, P. H. C.; Krishnan, V. Recent Advances in Plasmonic Photocatalysis Based on TiO<sub>2</sub> and Noble Metal Nanoparticles for Energy Conversion, Environmental Remediation, and Organic Synthesis. *Small* **2022**, *18*, No. 2101638.
- (69) Qiu, T.; Wang, L.; Zhou, B.; Zhu, Y.; Zhuang, C.; Liu, Q.; Shen, Q.; Xiong, Y.; Zhou, Y.; Zou, Z. Molybdenum Sulfide Quantum Dots Decorated on TiO<sub>2</sub> for Photocatalytic Hydrogen Evolution. *ACS Appl. Nano Mater.* **2022**, *5*, 702–709.
- (70) Liu, J.; Zheng, J.; Yue, G.; Li, H.; Liu, Z.; Zhao, Y.; Wang, N.; Sun, C.; Cui, Z. Continuous G-C<sub>3</sub>N<sub>4</sub> Layer-Coated Porous TiO<sub>2</sub> Fibers with Enhanced Photocatalytic Activity toward H<sub>2</sub> Evolution and Dye Degradation. *RSC Adv.* **2022**, *12*, 10258–10266.